Eur. Phys. J. C (2022) 82:481
https://doi.org/10.1140/epjc/s10052-022-10440-8

THE EUROPEAN PHYSICAL JOURNAL C

Regular Article - Theoretical Physics

Gravitational waves in models with multicritical-point principle

Yuta Hamada[1,a], **Hikaru Kawai**[2,3,b], **Kiyoharu Kawana**[4,c], **Kin-ya Oda**[5,d], **Kei Yagyu**[6,e]

[1] Department of Physics, Harvard University, Cambridge, MA 02138, USA
[2] Department of Physics and Center for Theoretical Physics, National Taiwan University, Taipei 106, Taiwan
[3] Physics Division, National Center for Theoretical Sciences, Taipei 10617, Taiwan
[4] Center for Theoretical Physics, Department of Physics and Astronomy, Seoul National University, Seoul 08826, Korea
[5] Department of Mathematics, Tokyo Woman's Christian University, Tokyo 167-8585, Japan
[6] Department of Physics, Osaka University, Toyonaka, Osaka 560-0043, Japan

Received: 29 March 2022 / Accepted: 15 May 2022 / Published online: 25 May 2022

Abstract The multicritical-point principle (MPP) provides a natural explanation of the large hierarchy between the Planck and electroweak scales. We consider a scenario in which MPP is applied to the Standard Model extended by two real singlet scalar fields ϕ and S, and a dimensional transmutation occurs by the vacuum expectation value of ϕ. In this paper, we focus on the critical points that possess a $\mathbb{Z}_2$ symmetry $S \to -S$ and all the other fields are left invariant. Then S becomes a natural dark matter (DM) candidate. Further, we concentrate on the critical points where ϕ does not possess further $\mathbb{Z}_2$ symmetry so that there is no cosmological domain-wall problem. Among such critical points, we focus on maximally critical one called CP-1234 that fix all the superrenormalizable parameters. We show that there remains a parameter region that satisfies the DM relic abundance, DM direct-detection bound and the current LHC constraints. In this region, we find a first-order phase transition in the early universe around the TeV-scale temperature. The resultant gravitational waves are predicted with a peak amplitude of $\mathcal{O}(10^{-12})$ at a frequency of $10^{-2}-10^{-1}$ Hz, which can be tested with future space-based instruments such as DECIGO and BBO.

1 Introduction

Gravitational Wave (GW) astronomy [1–3] is one of the most fascinating research fields because it allows us to explore the physics of the early universe, complementary to the cosmic microwave background (CMB) observations. Gravitational waves from compact binaries [4–6] and stochastic background [7–12] allow us to test new physics models as well as gravity theories. In particular, stochastic GWs originating from first-order phase transitions (FOPTs) [13–16] have received much attention in recent years, as many new physics models predict them in the early Universe, contrary to the pure Standard Model (SM), which shows a crossover electroweak (EW) transition [17,18].

In this paper, we study the FOPT and the resultant GW signals in an extension of the SM by two real singlet scalars ϕ and S that account for the hierarchy between the EW and Planck scales [19,20]. In the original Coleman–Weinberg (CW) mechanism [21,22], the scalar field has a loop-suppressed mass compared to its vacuum expectation value (VEV), and cannot be regarded as the observed Higgs boson at LHC. That is why ϕ must be introduced in addition to the SM Higgs as a scale-generating scalar. On the other hand, the role of the gauge field in the original CW model can be played by S [23]. In this sense, this model [19,20] can serve as a minimal model of the scale generation. As a bonus, we can naturally identify S as the weakly-interacting-massive-particle dark matter by imposing the $\mathbb{Z}_2$ symmetry $S \to -S$, with all other fields being invariant.

The starting assumption of the CW mechanism is the absence of dimensionful parameters, especially the scalar mass-squared, in the tree-level Lagrangian. This assumption is sometimes called the classical conformality or the classical scale invariance [24–39], and can be naturally explained [22,23] as a consequence of the multicritical-point principle (MPP) [40,41]. There are several ways to describe the MPP, but a simple one is "the coupling constants of a theory should be tuned to one of the multicritical points at which some of the extrema of the low-energy effective potential are degenerate". Here note that the consequences of the MPP do not

[a] e-mail: yhamada@fas.harvard.edu
[b] e-mail: hikarukawai@phys.ntu.edu.tw
[c] e-mail: kawana@snu.ac.kr (corresponding author)
[d] e-mail: odakin@lab.twcu.ac.jp
[e] e-mail: yagyu@het.phys.sci.osaka-u.ac.jp

depend on the renormalization scale μ because the effective potential exists independently of it, up to the renormalization of the field. See Refs. [19,20,22,42–49] for further discussion. In this sense, the MPP determines the couplings constants in the low-energy effective potential, and in particular, provides a natural answer to the fine-tuning problem.

Some of the mechanisms for realizing the MPP prefer criticalities with larger multiplicity [22,42,44]. In this paper, for the first time, we consider the two-scalar extension of the SM with maximal multicriticality in the sense that all the superrenormalizable couplings of the effective potential are fixed to a multicritical point, that is, all the relevant parameters in the low energy effective theory are fixed by the MPP.

As a first attempt, we focus on a class of multicritical points at which the Higgs mass-squared vanishes along with its superrenormalizable couplings to ϕ or S. The problem is then reduced to finding a maximally multicritical point of the two-scalar subsystem. Indeed in Ref. [22], the maximally multicritical points of the two-scalar system with the $\mathbb{Z}_2$ symmetry for S have already been classified. Among them, the so-called **1234** case (CP-1234 in this paper) is of particular interest because it can realize the FOPT without domain-wall problems around the TeV scale.

The organization of the paper is as follows. In Sect. 2, we discuss the maximal criticality at CP-1234 for the two-scalar extension of the SM. In Sect. 3, we study the FOPT by computing the bounce action and by obtaining the critical, nucleation, and percolation temperatures from it. In Sect. 4, we study the GW signals from the FOPT. We find that the phase-transition strength parameters are typically $\alpha = 10^{-2}-10^{-1}$ and $\beta/H = 10^{2}-10^{3}$. These values imply that the FOPT is not much strong and the resultant GW signals are dominated by the sound wave contributions. The resultant peak amplitude can be as large as $\mathcal{O}(10^{-12})$ around the frequency $10^{-2}-10^{-1}$ Hz, which can be tested by DECIGO and BBO. In Sect. 5, we provide a summary.

2 Model

We consider a model with two real singlet scalar fields ϕ and S in addition to the SM particles. To make S a dark matter candidate, we impose an unbroken $\mathbb{Z}_2$ symmetry whose transformation property is defined as $S \to -S$ and all the other fields to be even.[1]

The tree-level Lagrangian is

$$\mathcal{L} = \mathcal{L}_{\rm SM} + \frac{1}{2}(\partial_\mu \phi)^2 + \frac{1}{2}(\partial_\mu S)^2 - V(H, \phi, S), \tag{1}$$

where $\mathcal{L}_{\rm SM}$ is the SM Lagrangian without the Higgs potential for the SM doublet H. The scalar potential is generally given by

$$\begin{aligned} V(H,\phi,S) = {} & \frac{\lambda_H}{2}(H^\dagger H)^2 + \frac{\lambda_\phi}{4!}\phi^4 + \frac{\lambda_{\phi S}}{4}\phi^2 S^2 + \frac{\lambda_S}{4!}S^4 \\ & - \frac{\lambda_{\phi H}}{2}\phi^2(H^\dagger H) + \frac{\lambda_{SH}}{2}S^2(H^\dagger H) \\ & + \mu_H^2(H^\dagger H) + \frac{\mu_S^2}{2}S^2 + \mu_{\phi H}\phi H^\dagger H \\ & + \frac{\mu_{\phi S}}{2}\phi S^2 + \mu_1^3\phi \\ & + \frac{\mu_2^2}{2}\phi^2 + \frac{\mu_3}{3!}\phi^3. \end{aligned} \tag{2}$$

Here, the masses and couplings are the renormalized ones that appear in the low energy effective potential; we will discuss the concrete renormalization scheme in Eq. (4) and below.

We assume the *maximal* multicriticality, in which *all* the superrenormalizable parameters, i.e., the μ_i parameters given in the second line of Eq. (2), are fixed to one of the multicritical points in the parameter space by the MPP.

In particular, we focus on a class of multicritical points in which $(\mu_H, \mu_S, \mu_{\phi H}, \mu_{\phi S}, \mu_1, \mu_2, \mu_3)$ are fixed to be $(0, 0, 0, 0, \mu_1, \mu_2, \mu_3)$. The vanishing of the first four dimensionful parameters can be understood as follows. In the field space of (H, S, ϕ), we focus on the region where H and S are small, and rewrite the potential (2) as

$$\begin{aligned} V(H,\phi,S) = {} & \frac{\lambda_H}{2}(H^\dagger H)^2 + \frac{\lambda_\phi}{4!}\phi^4 + \frac{\lambda_S}{4!}S^4 + \frac{\lambda_{SH}}{2}S^2(H^\dagger H) \\ & - \frac{\lambda_{\phi H}}{2}\left[(\phi - \tilde{\mu}'_H)^2 + \tilde{\mu}_H^2\right](H^\dagger H) \\ & + \frac{\lambda_{\phi S}}{4}\left[(\phi - \tilde{\mu}'_S)^2 + \tilde{\mu}_S^2\right]S^2 \\ & + \mu_1^3\phi + \frac{\mu_2^2}{2}\phi^2 + \frac{\mu_3}{3!}\phi^3. \end{aligned} \tag{3}$$

The point with $\tilde{\mu}_H^2 = \tilde{\mu}_S^2 = 0$ in the parameter space is multicritical in the following sense (see also Ref. [19]): if $\tilde{\mu}_H^2 < 0$, then $\left[(\phi - \tilde{\mu}'_H)^2 + \tilde{\mu}_H^2\right]$ can change its sign when ϕ is varied, and stability and instability of H around $H = 0$ is flipped; on the other hand, if $\tilde{\mu}_H^2 > 0$, there is no such flip; in this sense $\tilde{\mu}_H^2 = 0$ is a critical point; the same argument holds for $\tilde{\mu}_S^2$. Hereafter, we choose such a multicritical point $\tilde{\mu}_H^2 = \tilde{\mu}_S^2 = 0$. Similarly, the point with $\tilde{\mu}'_H = \tilde{\mu}'_S$ in the parameter space is critical in the sense that both the H and S directions near their origin become simultaneously flat at the point $\phi = \tilde{\mu}'_H\ (= \tilde{\mu}'_S)$. Therefore, $\tilde{\mu}_H^2 = \tilde{\mu}_S^2 = 0$ and $\tilde{\mu}'_H = \tilde{\mu}'_S$ is a triple-critical point. After choosing this point, we may redefine $\phi - \tilde{\mu}'_H$ as a new ϕ. This corresponds to the point with $(0, 0, 0, 0, \mu_1, \mu_2, \mu_3)$ in the potential Eq. (2).

[1] This $\mathbb{Z}_2$ invariance can be viewed as a consequence of the MPP, as well as the maximal multicriticality that will be discussed below. In general, the existence of an accidental low-energy global symmetry can be viewed as a realization of multicriticality.

To obtain a maximal criticality, we need to fix the last three parameters (μ_1, μ_2, μ_3) to a maximal (triple-)critical point. Indeed, the classification of the two-scalar system of ϕ and S is given in Ref. [22]. Among the seven triple-critical points, the critical point **1234** (CP-1234) is of particular interest because it can realize the FOPT in the early universe without the domain-wall problem. We thus focus on the CP-1234 in this paper.

We briefly review the CP-1234 and the generalized CW mechanism [22,23]. The one-loop effective potential with $S = 0$ at zero temperature in the $\overline{\text{MS}}$ scheme is given by

$$\begin{aligned} V_{\text{eff}} &= \frac{\lambda_H}{2}(H^\dagger H)^2 - \frac{\lambda_{\phi H}}{2}\phi^2(H^\dagger H) + \mu_1^3\phi + \frac{\mu_2^2}{2}\phi^2 \\ &\quad + \frac{\mu_3}{3!}\phi^3 + \frac{\lambda_\phi}{4!}\phi^4 \\ &\quad + \frac{m_\phi^4(\phi)}{64\pi^2}\ln\left(\frac{m_\phi^2(\phi)}{\mu^2 e^{3/2}}\right) + \frac{m_S^4(\phi)}{64\pi^2}\ln\left(\frac{m_S^2(\phi)}{\mu^2 e^{3/2}}\right) \\ &\quad + \Delta V_{\text{1-loop}}(h,\mu), \end{aligned} \tag{4}$$

where $\Delta V_{\text{1-loop}}(h,\mu)$ is the one-loop potential for the physical Higgs h at the renormalization scale μ, and the effective masses are given by

$$m_\phi^2(\phi) = \mu_2^2 + \mu_3\phi + \frac{\lambda_\phi}{2}\phi^2, \quad m_S^2(\phi) = \frac{\lambda_{\phi S}}{2}\phi^2. \tag{5}$$

In Eq. (4), we have neglected the H-loop contribution to the ϕ potential because we focus on the parameter region $\lambda_{\phi H} \ll \lambda_{\phi S}$. Also, the H dependence in Eq. (5) are neglected because we consider the region $\lambda_{\phi H} H^\dagger H \ll \lambda_\phi \phi^2$ and $\lambda_{SH} H^\dagger H \ll \lambda_{\phi S}\phi^2$. We choose the renormalization scale $\mu = \tilde{M}$ at which $\lambda_\phi = 0$ [22]:

$$\begin{aligned} V_{\text{eff}} &= \frac{\lambda_H}{2}(H^\dagger H)^2 - \frac{\lambda_{\phi H}}{2}\phi^2(H^\dagger H) + \Delta V_{\text{1-loop}}(h,\tilde{M}) \\ &\quad + \frac{m_\phi^4(\phi)}{64\pi^2}\ln\left(\frac{m_\phi^2(\phi)}{\tilde{M}^2 e^{3/2}}\right) + V_\phi(\phi), \end{aligned} \tag{6}$$

where

$$V_\phi(\phi) = \mu_1^3\phi + \frac{\mu_2^2}{2}\phi^2 + \frac{\mu_3}{3!}\phi^3 + \frac{c}{48}\phi^4\ln\left(\frac{\phi^2}{M^2}\right), \tag{7}$$

in which

$$c = \frac{3\lambda_{\phi S}^2}{16\pi^2}, \quad M^2 = \frac{2\tilde{M}^2 e^{3/2}}{\lambda_{\phi S}}. \tag{8}$$

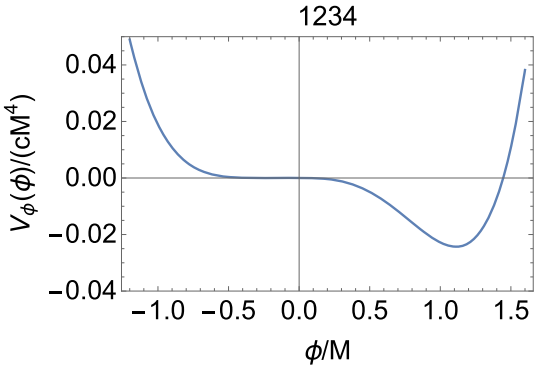

Fig. 1 Shape of the potential $V_\phi(\phi)$ normalized by cM^4 at the CP-1234

By neglecting the $m_\phi^4(\phi)$ term in Eq. (6), the CP-1234 is realized as

$$\left.\frac{dV_\phi}{d\phi}\right|_{\phi=\phi_S} = \left.\frac{d^2V_\phi}{d\phi^2}\right|_{\phi=\phi_S} = \left.\frac{d^3V_\phi}{d\phi^3}\right|_{\phi=\phi_S} = \left.\frac{d^4V_\phi}{d\phi^4}\right|_{\phi=\phi_S} = 0 \tag{9}$$

at the field point $\phi = \phi_S$. These conditions completely fix the parameters of $V_\phi(\phi)$ as

$$\begin{aligned} &\mu_1^3 = -\frac{c}{18}M^3 e^{-\frac{25}{4}}, \quad \mu_2^2 = -\frac{c}{4}M^2 e^{-\frac{25}{6}}, \\ &\mu_3 = -cMe^{-\frac{25}{12}}, \quad \phi_S = -Me^{-\frac{25}{12}}. \end{aligned} \tag{10}$$

Note that μ_1^3, μ_2^2, and μ_3 are proportional to the one-loop suppression factor c. This is consistent with having neglected the $m_\phi^4(\phi)$ term because $m_\phi^2(\phi)$ is proportional to c as we have chosen the renormalization point such that $\lambda_\phi = 0$. Substituting Eq. (10) into Eq. (7), we obtain

$$\begin{aligned} V_\phi(\phi) &= cM^4\left[-\frac{\bar{\phi}}{18e^{25/4}} - \frac{\bar{\phi}^2}{8e^{25/6}} - \frac{\bar{\phi}^3}{6e^{25/12}} + \frac{\bar{\phi}^4}{48}\ln\bar{\phi}^2\right], \\ \bar{\phi} &:= \frac{\phi}{M}. \end{aligned} \tag{11}$$

The corresponding potential is shown in Fig. 1.

The VEV v_ϕ at the true vacuum and the mass of ϕ are numerically found to be

$$v_\phi = 1.1M, \quad m_\phi^2 = -\frac{\lambda_{\phi H}}{2}v^2 + 0.28cM^2. \tag{12}$$

The EW symmetry breaking is triggered by the mixing coupling $\lambda_{\phi H}$, and the Higgs VEV is

$$v := \sqrt{2}\langle H\rangle = v_\phi\sqrt{\frac{\lambda_{\phi H}}{\lambda_H}}, \tag{13}$$

where $v \simeq 246$ GeV. In the EW vacuum, the physical scalar states $\hat{h}$ and $\hat{h}_\phi$, which are defined as $\hat{h} = \sqrt{2}\mathrm{Re}H^0 - v$ and $\hat{h}_\phi = \phi - v_\phi$, are mixed with each other. The squared mass matrix in the basis of $(\hat{h}, \hat{h}_\phi)$ is given by

$$\mathcal{M}^2 = v^2 \begin{pmatrix} \lambda_H & -\frac{v}{v_\phi}\lambda_H \\ -\frac{v}{v_\phi}\lambda_H & \frac{m_\phi^2}{v^2} \end{pmatrix}. \tag{14}$$

By introducing the mixing angle θ, the mass eigenstates of the Higgs bosons (h, h_ϕ) are defined as

$$\begin{pmatrix} \hat{h} \\ \hat{h}_\phi \end{pmatrix} = \begin{pmatrix} \cos\theta & -\sin\theta \\ \sin\theta & \cos\theta \end{pmatrix} \begin{pmatrix} h \\ h_\phi \end{pmatrix}, \tag{15}$$

and their squared masses and θ are expressed as

$$m_h^2 = \mathcal{M}_{11}^2 \cos^2\theta + \mathcal{M}_{22}^2 \sin^2\theta - \mathcal{M}_{12}^2 \sin 2\theta, \tag{16}$$

$$m_{h_\phi}^2 = \mathcal{M}_{11}^2 \sin^2\theta + \mathcal{M}_{22}^2 \cos^2\theta + \mathcal{M}_{12}^2 \sin 2\theta, \tag{17}$$

$$\tan 2\theta = \frac{2\mathcal{M}_{12}^2}{\mathcal{M}_{11}^2 - \mathcal{M}_{22}^2}. \tag{18}$$

On the other hand, S does not mix with $\hat{h}$ and $\hat{h}_\phi$ due to the $\mathbb{Z}_2$ parity, and so its squared mass is simply determined to be

$$m_S^2 = \frac{1}{2}(v^2\lambda_{SH} + v_\phi^2\lambda_{\phi S}). \tag{19}$$

From the above discussion, two of the six dimensionless parameters $\lambda_H, \lambda_\phi, \lambda_S, \lambda_{\phi S}, \lambda_{\phi H}$, and λ_{SH} in the potential are fixed by v and the Higgs mass $m_h \simeq 125$ GeV. For simplicity, we choose λ_S to be zero at the EW scale, since it does not play a phenomenologically important role. Thus, we can choose the free parameters as

$$\{m_S,\ \lambda_{SH},\ \lambda_{\phi S}\} \text{ or } \{m_S,\ \lambda_{SH},\ v_\phi\}. \tag{20}$$

In the latter, the input parameter $\lambda_{\phi S}$ is exchanged by v_ϕ via Eq. (19). Among these couplings, $\lambda_{\phi S}$ is the most important one for the discussion of the FOPT because it determines the finite temperature potential of ϕ.

As aforementioned, S is the dark matter candidate in this model. Its thermal relic abundance and the constraint from direct searches at XENON1T [50] have been investigated in Ref. [19] for some of double-critical points in the $(\mu_1^3, \mu_2^2, \mu_3)$ space. On the other hand, we study the maximal (triple-)critical point in the current paper. The differences in the predictions of m_{h_ϕ} and θ from the previous analysis solely originate from the numerical factor 0.28 in Eq. (12). The current maximally critical model tends to predict a slightly larger mass of h_ϕ compared with the previous one. This makes the bound from the direct search slightly weaker. On the other hand, the relic abundance is well fitted by the following formula [19]:

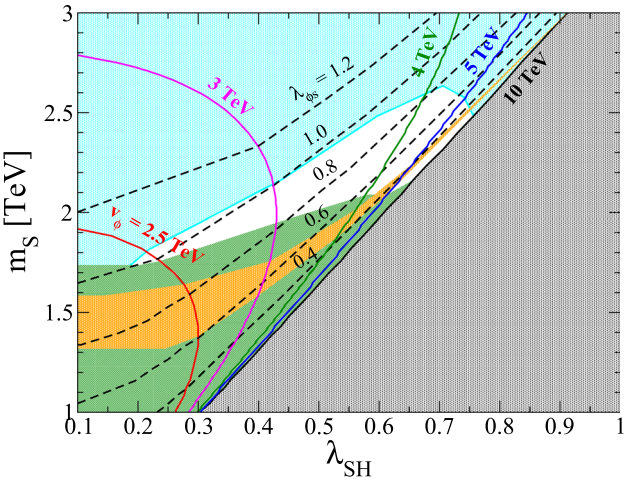

Fig. 2 Allowed parameter region (non-shaded) satisfying the observed relic abundance of dark matter on the λ_{SH}–m_S plane. Each of the solid and dashed curves shows the fixed value, written along the curve, of v_ϕ and $\lambda_{\phi S}$, respectively. Shaded regions are respectively excluded by the XENON1T experiment (green), the LHC data (orange), dark matter abundance (gray), and the perturbativity bound (cyan). Regarding the perturbativity bound, the absence of Landau pole up to $\mu = 10^{17}$ GeV is imposed

$$4\lambda_{SH}^2 + \lambda_{\phi S}^2 = \left(\frac{m_S}{m_{\rm th}}\right)^2, \quad m_{\rm th} = 1590 \pm 40 \text{ GeV}. \tag{21}$$

We note that in the numerical evaluation of the relic abundance and the constraint from the direct search, we employ the `MicrOMEGAs` package [51], and impose the relic abundance to be $\Omega_S h^2 = 0.12$ [52].

In Fig. 2, we show the regions allowed (non-shaded area) by various constraints on the λ_{SH}–m_S plane. Each point in the allowed region satisfies the relic abundance, i.e., v_ϕ and $\lambda_{\phi S}$ are determined such that they satisfy Eqs. (19) and (21). The solid and dashed curves respectively show the contours of fixed values of v_ϕ and $\lambda_{\phi S}$, where the number is written along each curve. We also show the other constraints on the model parameters in the figure: The green, orange, gray, and cyan shaded regions are excluded by the updated XENON1T result [50],[2] the LHC data, dark matter relic abundance, and perturbativity bound, respectively [19]. For the LHC bound, we demand that the signal strength of the Higgs boson μ_h is given within the 2σ range, where the current measurement with the integrated luminosity of 139 fb^{-1} shows $\mu_h = 1.06 \pm 0.06$ [53]. In our scenario, μ_h can differ from unity due to the mixing with the singlet-like Higgs boson h_ϕ, so this constraint

[2] For the region with the dark matter mass larger than 1 TeV, we extrapolate the upper limit on the spin-independent cross-section for dark matter and nucleon scatterings.

can be described as $\sin^2\theta \leq 0.06$. We see that the successful benchmark scenario is given at the well constrained region, i.e., $1.7\,\text{TeV} \lesssim m_S \lesssim 2.5\,\text{TeV}$, $0.2 \lesssim \lambda_{SH} \lesssim 0.75$, and $0.4 \lesssim \lambda_{\phi S} \lesssim 0.8$. In Table 1, we show the range of parameters allowed by all the constraints discussed above for each fixed value of v_ϕ.

3 First order phase transition

In this section, we estimate the bubble nucleation and percolation temperatures of the FOPT using the effective potential of ϕ at finite temperature. For the model described in Sect. 2, we will see that the potential barrier disappears below $T = 0.26\,T_c$ due to the existence of the linear term in the zero-temperature effective potential (6), where T_c is the critical temperature at which the free energies of two vacua become degenerate. This implies that the percolation temperature cannot fall below $0.26\,T_c$. In Sect. 3.1, we study the effective potential of ϕ at finite temperature. We then discuss the nucleation and percolation in Sect. 3.2.

3.1 Finite temperature potential

Let us study the one-loop effective potential at finite temperature. In general, the one-loop thermal correction is

$$V_{\rm th}^{\text{1-loop}}(\phi, T) = \frac{T^4}{2\pi^2}\sum_i \left[g_{{\rm B}i} I_{\rm B}\left(\frac{m_{{\rm B}i}(\phi)}{T}\right) - g_{{\rm F}i} I_{\rm F}\left(\frac{m_{{\rm F}i}(\phi)}{T}\right)\right], \tag{22}$$

where $g_{{\rm B}i}$ and $m_{{\rm B}i}$ ($g_{{\rm F}i}$ and $m_{{\rm F}i}$) represent the degrees of freedom and mass for boson (fermion), respectively, and the functions $I_{\rm B}$ and $I_{\rm F}$ are given by

$$I_{B/F}(a) = \int_0^\infty dx x^2 \log\left(1 \mp e^{-\sqrt{x^2+a^2}}\right). \tag{23}$$

In principle, all the scalar fields may contribute to the one-loop potential of ϕ. However, the contributions from H and ϕ are smaller than from S because $m_H^2(\phi) \ll m_S^2(\phi)$ and $m_\phi^2(\phi) \ll m_S^2(\phi)$ as discussed below Eqs. (5) and (10). Thus, it suffices to take into account the S contribution only:[3]

$$V_{\rm eff}(\phi, T) = V_\phi(\phi) + \frac{T^4}{2\pi^2} I_{\rm B}\left(\frac{m_S(\phi)}{T}\right)$$

$$m_S^2(\phi) = \frac{\lambda_{\phi S}}{2}\phi^2. \tag{24}$$

At high temperatures, the perturbative calculations may break down, and it is necessary to sum up all the relevant diagrams [54,55]. The so-called daisy resummation in the Parwani scheme [56] can be obtained by simply replacing $m_S(\phi)$ with the thermal corrected effective mass $m_S^{\rm daisy}(\phi, T)$:

$$V_{\rm eff}^{\rm daisy}(\phi, T) = V_\phi(\phi) + \frac{T^4}{2\pi^2} I_{\rm B}\left(\frac{m_S^{\rm daisy}(\phi, T)}{T}\right), \tag{25}$$

where

$$\left(m_S^{\rm daisy}(\phi, T)\right)^2 = m_S^2(\phi) + \frac{\lambda_{\phi S} T^2}{2} J\left(\frac{m_S^2(\phi)}{T^2} + \frac{\lambda_{\phi S}}{24}\right), \tag{26}$$

$$J(\alpha) := \frac{1}{\pi^2}\frac{\partial}{\partial\alpha} I_{\rm B}(\alpha) = \frac{1}{12} - \frac{\alpha^{1/2}}{4\pi} + \cdots. \tag{27}$$

In the upper-left panel in Fig. 3, we show $V_{\rm eff}(\phi, T)$ (curves) and $V_{\rm eff}^{\rm daisy}(\phi, T)$ (dots) for different values of T. Although there actually exist tiny differences between these potentials, the difference is less than 1% even when $T/T_c \sim 1$ (T_c is $\sim 0.28M$ from the figure). Therefore, we use $V_{\rm eff}(\phi, T)$ in the following discussion.

To understand the parameter dependence of the FOPT, it is convenient to normalize the effective potential by cM^4:

$$\overline{V}_{\rm eff}(\bar\phi, \tau) := \frac{V_{\rm eff}(\phi, T)}{cM^4} = -\frac{\bar\phi}{18e^{25/4}} - \frac{\bar\phi^2}{8e^{25/6}} - \frac{\bar\phi^3}{6e^{25/12}} + \frac{\bar\phi^4}{48}\log\bar\phi^2 + \frac{2\tau^4}{3} I_{\rm B}\left(\frac{\bar\phi}{\tau}\right), \tau := \frac{T}{m_S(M)}. \tag{28}$$

One can see that the parameter dependence of the effective potential appears only through τ except for the overall normalization so that the critical behavior is determined only by the τ parameter. In the upper right panel in Fig. 3, we plot $\overline{V}_{\rm eff}$ where the different colors correspond to the different values of τ. The critical value of τ, i.e., τ_c at which the two vacua are degenerate is numerically found to be

$$\tau_c = 0.39, \tag{29}$$

by which the critical temperature T_c is determined to be

$$T_c = 0.39\, m_S(M), \tag{30}$$

and hence $\tau = 0.39\, T/T_c$.

There is another important value of τ, denoted by τ_b, at which the potential barrier disappears due to the linear term

[3] In fact, the background mass of ϕ is $m_\phi^2(\phi) = \mu_2^2 + \mu_3\phi/3 \propto \lambda_{\phi S}^2/16\pi^2$, from which we can estimate the mass ratio at around $\phi = M$ as $m_\phi^2(M)/m_S^2(M) \sim \lambda_{\phi S}/16\pi^2 \lesssim 0.06$ for $\lambda_{\phi S} \lesssim 1$. Thus, the contribution from ϕ is at most 10% of that from S.

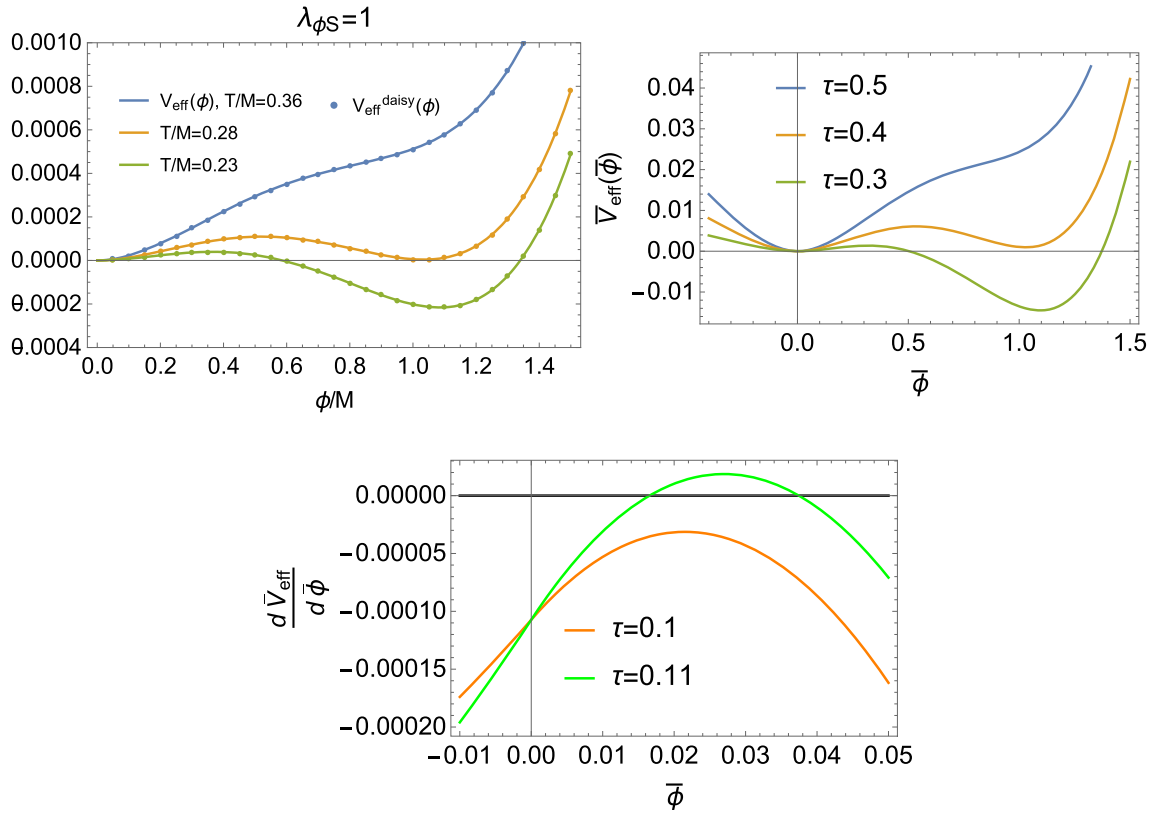

Fig. 3 Upper left: Comparison between $V_{\rm eff}(\phi, T)$ (curves) and $V_{\rm eff}^{\rm daisy}(\phi, T)$ (dots). Upper right: Normalized effective potential $\overline{V}_{\rm eff}(\overline{\phi}; \tau)$. Lower: The $\overline{\phi}$-derivative of $\overline{V}_{\rm eff}(\overline{\phi}; \tau)$

of the potential V_ϕ at zero temperature. The value of $\tau_{\rm b}$ is numerically found to be

$$\tau_{\rm b} = 0.10, \tag{31}$$

which corresponds to

$$T_{\rm b} = 0.10\, m_S(M) \simeq 0.26\, T_{\rm c}. \tag{32}$$

For illustration, in the lower panel of Fig. 3, $d\overline{V}_{\rm eff}/d\overline{\phi}$ is shown for $\tau = 0.1$ (orange) and $\tau = 0.11$ (green). When $\tau = 0.11$, the derivative of the potential is always negative, which means that there is no potential barrier in this case. When temperature is $T_{\rm n} \lesssim T \lesssim T_{\rm c}$, the universe is supercooled, where $T_{\rm n}$ is the bubble nucleation temperature. In the present case however, there is not large room for the supercooling because $T_{\rm b} = 0.26\, T_{\rm c}$.

3.2 Nucleation and percolation

We estimate the bubble nucleation and percolation temperatures. The dynamics of phase transition is determined by the decay rate of the false vacuum into the true vacuum per unit time and volume:

$$\Gamma(T) \sim T^4 \exp\left(-\frac{S_3(T)}{T}\right), \tag{33}$$

where S_3 is the $O(3)$-symmetric bounce action. The bubble nucleation is realized when

$$\frac{\Gamma(T_{\rm n})}{\left(H(T_{\rm n})\right)^4} \sim 1, \tag{34}$$

where $H(T)$ is the Hubble scale at temperature T. In the radiation-dominated era, $H(T)$ is given by (see e.g. Ref. [57])

$$H(T) = 1.66\sqrt{g_*}\frac{T^2}{M_{\rm P}}, \tag{35}$$

where $g_* \sim 100$ is the effective number of massless degrees of freedom and $M_{\rm P} = 1.2 \times 10^{19}$ GeV is the Planck mass. To estimate the nucleation temperature $T_{\rm n}$, we evaluate S_3 at temperature T given by

$$S_3 = \frac{4\pi M}{\sqrt{c}} \int_0^\infty d\rho \rho^2 \left[\frac{1}{2}\left(\frac{d\overline{\phi}_{\rm B}}{d\rho}\right)^2 + \overline{V}_{\rm eff}(\overline{\phi}_{\rm B}; \tau)\right], \tag{36}$$

where ρ is the normalized radial coordinate of the 3-dimensional Euclidean space r defined by $\rho = c^{1/2}Mr$. In Eq. (36), $\bar{\phi}_{\rm B}$ is the bounce solution of $\bar{\phi}$ satisfying the following equation of motion:

$$\frac{d^2\bar{\phi}_{\rm B}}{d\rho^2} + \frac{2}{\rho}\frac{d\bar{\phi}_{\rm B}}{d\rho} = \frac{\partial \overline{V}_{\rm eff}}{\partial\bar{\phi}}\Big|_{\bar{\phi}=\bar{\phi}_{\rm B}}, \quad \bar{\phi}_{\rm B}(\infty) = \bar{\phi}_{\rm FV}, \quad \frac{d\bar{\phi}_{\rm B}}{d\rho}\Big|_{\rho=0} = 0, \tag{37}$$

where $\bar{\phi}_{\rm FV}$ is the location of the false vacuum near the origin, which is numerically obtained for each τ.

After the bubble nucleation, there is a temperature at which true vacuum bubbles start to form an infinite connected cluster. Such a temperature is referred to as the percolation temperature $T_{\rm p}$, which is customary estimated by [58]

$$I(T_{\rm p}) \sim 0.34, \tag{38}$$

where $I(T)$ is the exponent of the probability of finding a point still in the false vacuum: $p(T) = e^{-I(T)}$. It is given by

$$I(T) = \int_{t_{\rm c}}^{t} dt'\Gamma(t')a(t')^3 \times \frac{4\pi}{3}R(t,t')^3,$$
$$R(t,t') = v_{\rm w}\int_{t'}^{t}\frac{ds}{a(s)}, \tag{39}$$

where $a(t)$ and $v_{\rm w}$ are the scale factor at time t and the bubble wall velocity, respectively. The determination of $v_{\rm w}$ is one of the challenging issues in the field of FOPTs [59]. We choose $v_{\rm w} = 0.5$ [60,61] as a benchmark value in this paper. For numerical evaluations, we determine $T_{\rm n}$ and $T_{\rm p}$ by assuming that Eqs. (33), (34), and (38) exactly hold. When $g_* = 100$ and $M_{\rm P}/T_{\rm n} = 10^{17}$, the condition for $T_{\rm n}$ can be expressed as $S_3/T_{\rm n} \simeq 145$.

In the left panel in Fig. 4, we plot the numerical values of $S_3(T)/T$ for $\lambda_{\phi S} = 0.6$ by using the `FindBounce` package [62].[4] Here, the gray region represents $\tau < \tau_{\rm b}$ $(= 0.10)$ $\leftrightarrow T/T_{\rm c} < 0.25$, where the potential barrier no longer exists.

In the right panel in Fig. 4, we plot $T_{\rm c}$ (blue), $T_{\rm n}$ (orange), and $T_{\rm p}$ (green points) as functions of $\lambda_{\phi S}$ for $v_\phi = 3$ TeV and $v_{\rm w} = 0.5$. As in the left panel, the potential barrier disappears in the gray region. One can see that there is no significant difference between $T_{\rm n}$ and $T_{\rm p}$ in the present model, which means that the percolation occurs soon after the onset of nucleation. Note also that $T_{\rm n}$ and $T_{\rm p}$ become smaller than $T_{\rm b}$ for $\lambda_{\phi S} \lesssim 0.4$. We have checked that this is the case for 3 TeV $\lesssim v_\phi \lesssim$ 10 TeV. In particular for $v_\phi = 10$ TeV, a FOPT cannot be realized consistent with other phenomenological constraints because the allowed region of $\lambda_{\phi S}$ is smaller than 0.4 (see Table 1).

[4] As a consistency check, we have also calculated the bounce action by using the `CosmoTransitions` [63] and obtained the same results within a few percent accuracy.

4 Gravitational wave signals

In this section, we study the GW signals produced by the FOPT. In general, there are three kinds of sources of the stochastic GWs produced during a FOPT: bubble collisions, sound waves, and magnetohydrodynamic (MHD) turbulence in the plasma [60,61]. Typically, the dominant source is the sound waves as long as the FOPT is not too strong, i.e., $\alpha \lesssim 1$ and $\beta/H \gtrsim 100$ in the following notation.

4.1 Strength parameters

There are two important parameters, α and β, to determine the GW energy spectrum $\Omega_{\rm GW}(f)$ produced by a FOPT. The parameter α measures the strength of the FOPT, which is conventionally defined by the ratio between the latent heat energy and the radiation energy $\rho_{\rm R}$:

$$\alpha(T) = \frac{\Delta e(T)}{\rho_R(T)} = \frac{1}{\rho_{\rm R}(T)}\left[\Delta V_{\rm eff}(T) - T\frac{\partial \Delta V_{\rm eff}(T)}{\partial T}\right], \tag{40}$$

where

$$\Delta V_{\rm eff}(T) = V_{\rm eff}(\phi_{\rm false}, T) - V_{\rm eff}(\phi_{\rm true}, T) := -\Delta p(T). \tag{41}$$

We note that the second term in Eq. (40), i.e., the contribution from the difference of entropy, is negligibly smaller than the first term. On the other hand, the recent study [64] suggests that we should use the pseudotrace of fluid energy-momentum tensor to define the strength parameter:

$$\alpha_{\bar{\theta}} = \frac{\Delta e(T) - \Delta p(T)/c_s^2}{4\rho_R(T)}, \tag{42}$$

where c_s is the sound velocity.

The other parameter β is defined by

$$\beta(T) := -H(T)T\frac{\partial \ln\Gamma(T)}{\partial T}, \tag{43}$$

which determines the duration of the FOPT and the characteristic frequency of the GWs. In the following, we will consider two commonly assumed options $T = T_{\rm p}$ and $T = T_{\rm n}$ for the typical temperature to evaluate α and β [60,61,65].

In Fig. 5, we show our numerical results in the α–β plane for $v_\phi = 3$ TeV (left), $v_\phi = 4$ TeV (middle), and $v_\phi = 5$ TeV (right), where $\lambda_{\phi S}$ is varied in each contours within the range $0.4 \le \lambda_{\phi S} \le 1$. The orange and blue colors correspond to the choices $T = T_{\rm p}$ and $T = T_{\rm n}$ respectively, and the solid (dashed) lines correspond to Eq. (40) (Eq. (42) with $c_s^2 = 1/3$.). The orders of magnitude of α and β/H are 0.1–0.4 and 10^2–10^3, respectively, indicating that the FOPT is moderate

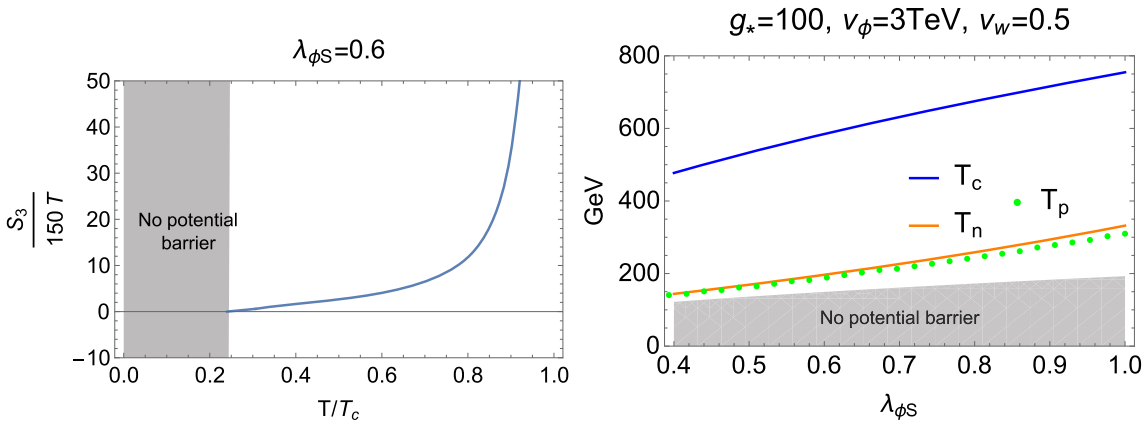

Fig. 4 Left: Bounce action $S_3(T)/T$. Right: Various temperatures: The blue and orange lines are the critical and nucleation temperatures T_c and T_n, respectively, and the green points are the percolation temperature T_p. In both panels, gray region is $T < T_b = 0.25T_c$

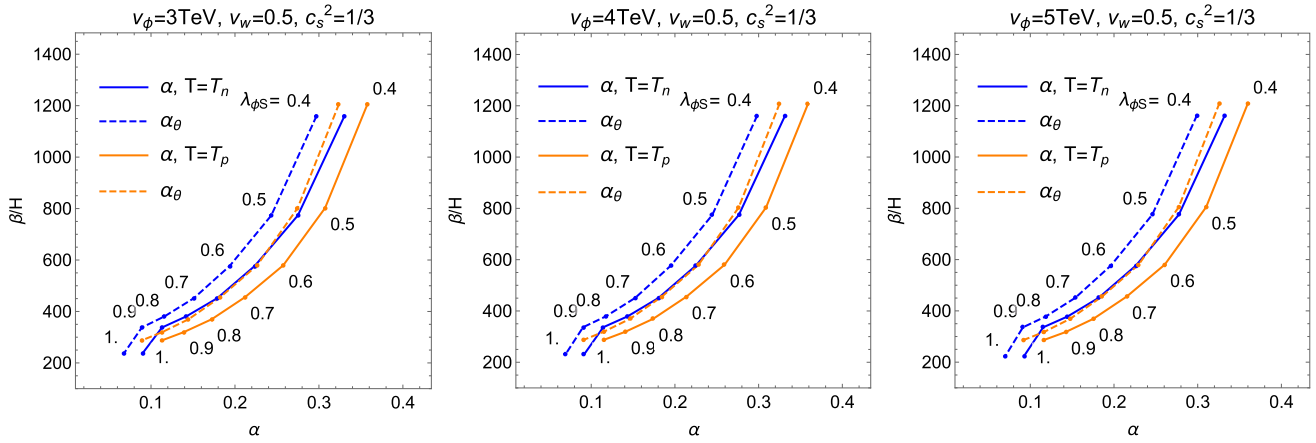

Fig. 5 Predictions of α and β/H for $v_\phi = 3$ TeV (left), $v_\phi = 4$ TeV (middle), and $v_\phi = 5$ TeV (right). Here the solid (dashed) lines correspond to Eq. (40) (Eq. (42)) respectively

in this model. In particular, the large β/H corresponds to the short duration of the FOPT, and this is why T_n and T_p are close to each other as seen in the previous section. For the calculations of GW spectrum, we will use α_θ conservatively.

To obtain the GW spectrum, we also need to calculate the energy efficiency factor κ_v which is defined as the fraction of vacuum energy that is transferred to the bulk motion of plasma. In this paper, we use the analytical fitting result presented in Ref. [66]:

$$\kappa_v = \frac{c_s^{11/5}\kappa_A\kappa_B}{(c_s^{11/5} - v_w^{11/5})\kappa_B + v_w c_s^{6/5}\kappa_A} \quad (\text{for } v_w \lesssim c_s = 1/\sqrt{3}), \quad (44)$$

where $c_s \sim 0.58$ is the speed of sound and

$$\kappa_A = v_w^{6/5}\frac{6.9\alpha}{1.36 - 0.037\sqrt{\alpha} + \alpha},$$
$$\kappa_B = \frac{\alpha^{2/5}}{0.017 + (0.997 + \alpha)^{2/5}}. \quad (45)$$

4.2 Gravitational wave signals

We now have all the necessary inputs to calculate the GW signals from the FOPT. In this paper, we rely on the numerical fitting functions presented in Ref. [60]. Here, let us once again clarify the relevant parameters in our model. As discussed above, the strength parameters $(\alpha_{\tilde{\theta}}, \beta)$ are functions of $\lambda_{\phi S}$ and v_ϕ, and they are constrained by the XENON1T experiment and the theoretical perturbativity bound. In particular, only a finite range of $\lambda_{\phi S}$ is allowed for a given fixed value of v_ϕ as shown in Table 1.

In Fig. 6, we show the GW energy spectra for $v_\phi = 3$ TeV (upper left), 4 TeV (upper right), and 5 TeV (lower). For each v_ϕ, the results of taking the minimum and maximum allowed values of $\lambda_{\phi S}$ are shown as dashed and solid blue lines, respectively. Here, the other parameters are chosen as

$$v_w = 0.5, \quad \epsilon = 0.05, \quad (46)$$

Table 1 Range of parameters allowed by all the constraints

v_ϕ (TeV)	λ_{SH}	$\lambda_{\phi S}$	m_S (GeV)	m_{h_ϕ} (GeV)	$\sin\theta$
2.5	(0.21, 0.24)	(0.99, 1.1)	(1760, 1810)	(160, 170)	(0.11, 0.13)
3	(0.42, 0.43)	(0.84, 1.0)	(1950, 2140)	(170, 200)	(0.052, 0.10)
4	(0.58, 0.68)	(0.54, 0.84)	(2090, 2600)	(140, 220)	(0.029, 0.18)
5	(0.66, 0.74)	(0.40, 0.53)	(2250, 2570)	(140, 170)	(0.053, 0.24)
10	(0.65, 0.76)	(0.093, 0.12)	(2160, 2480)	(60, 80)	$(-0.042, -0.032)$

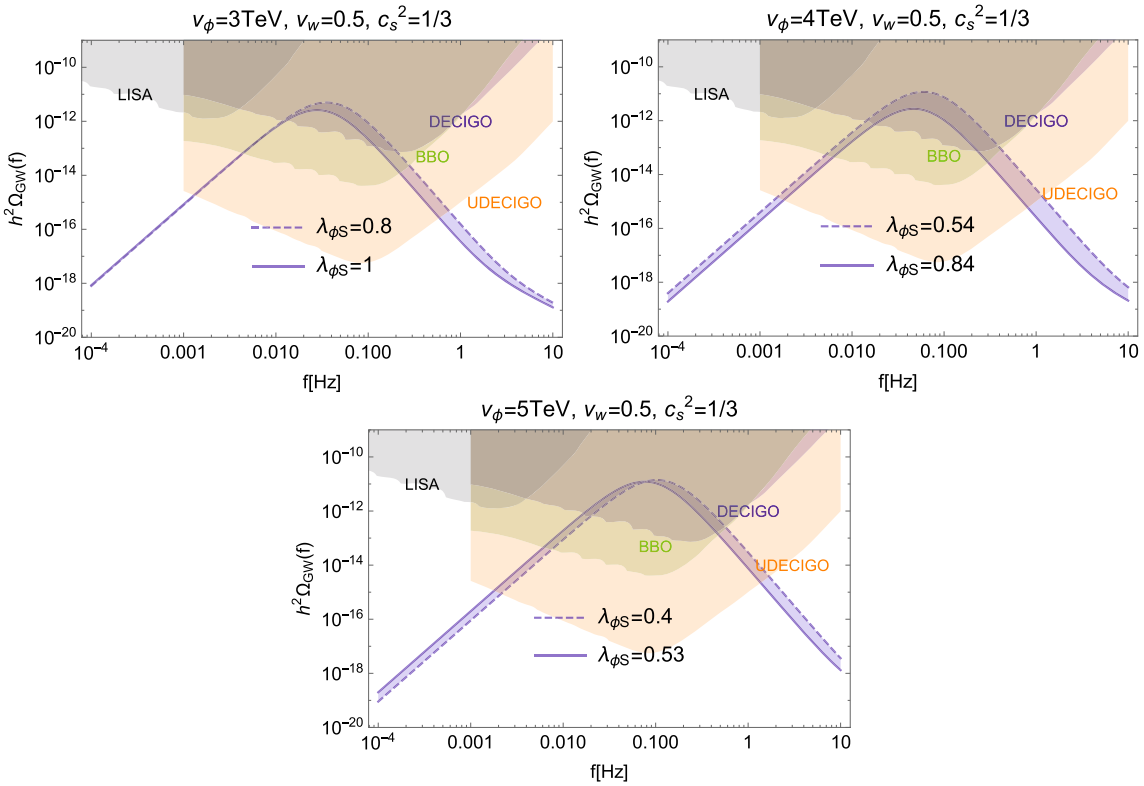

Fig. 6 GW spectra for $v_\phi = 3$ TeV (upper left), 4 TeV (upper right), and 5 TeV (lower). For each v_ϕ, the results of taking the minimum and maximum allowed values of $\lambda_{\phi S}$ are shown as dashed and solid blue lines, respectively. The colored regions show the sensitivity curves for various future detectors

where ϵ denotes the energy fraction of the turbulent bulk motion. The colored regions show the sensitivity curves of future detectors. One can see that the peak amplitudes can become as large as $\mathcal{O}(10^{-12})$ with a peak frequency 10^{-2}–10^{-1} Hz, which can be tested by DECIGO andbreak BBO.[5]

[5] In Refs. [61,67], it was pointed out that the sound wave signals can be severely reduced due to the short duration of a FOPT. Additional reduction of the GW signals is given by $(8\pi)^{1/3}K^{-1/2}\mathrm{Max}(v_w, c_s)(H_*/\beta)$ where $K = \kappa_v\alpha/(1+\alpha)$, and this becomes ~ 0.03 for $\alpha = 0.1$, $\beta/H_* = 400$, and $v_w = 0.5$. As a result, the peak amplitudes may not reach the sensitivity curve of DECIGO. However, since there are still many ambiguities such as the wall velocity, more dedicated studies are necessary to predict the GW signals more accurately.

5 Summary

As a minimal model to explain the electroweak scale that is exponentially smaller than the Planck scale, we have proposed the two-scalar extension of the SM with maximal multicriticality in the sense that all the superrenormalizable parameters of the scalar potential are fixed by the MPP. As a first trial, we focused on the class of criticalities in which S has the $\mathbb{Z}_2$ symmetry $S \to -S$, the masses squared of H and S vanish, and the cubic couplings $\phi H^\dagger H$ and ϕS^2 vanish too. Then we can employ the classification of the maximally multicritical points of the two-scalar sector of ϕ and S in Ref. [22]. Among them, the so-called CP-1234 case is phenomenologically interesting, in which S acts as dark matter, and a FOPT can occur around the electroweak scale in the early universe.

In this paper, we have studied the dark matter abundance and the constraints from its direct detection as well as from the LHC data and the theoretical perturbativity bound. As a result, we have found an allowed region with the masses of dark matter m_S and the additional neutral scalar boson m_{h_ϕ} to be $1.8\,\text{TeV} \lesssim m_S \lesssim 2.5\,\text{TeV}$ and $60\,\text{GeV} \lesssim m_S \lesssim 220\,\text{GeV}$, respectively. In addition, the coupling constants are constrained to be $0.2 \lesssim \lambda_{SH} \lesssim 0.8$ and $0.1 \lesssim \lambda_{\phi S} \lesssim 1.1$. Then, we have studied the FOPT and the resultant GW signals. One of the interesting features of the maximum criticality is the presence of the linear term in the ϕ potential, which ensures that the system does not have a long supercooling period. We have calculated the phase-transition strength parameters and found $\alpha = 10^{-2}-10^{-1}$ and $\beta/H = 10^{2}-10^{3}$ within the allowed region of parameters summarized above. These moderate values of strength parameters imply that the GW signals are dominated by sound wave contributions. We have found that the peak amplitude can become as large as $\mathcal{O}(10^{-12})$ around the frequency $10^{-2}-10^{-1}\,\text{Hz}$, which can be tested by future detectors such as DECIGO and BBO.

It would be interesting to study more general multicritical points of the two-scalar extension of the SM. As a different extension of the SM, the roles of ϕ and S for the electroweak-scale generation can be played by a singlet complex scalar and another doublet Higgs, respectively. If this model has the Peccei–Quinn (PQ) symmetry [68–76], it can be the DFSZ axion model. In general, PQ symmetry is difficult to impose because it is violated by anomalies at the ultraviolet cutoff scale. However, the MPP can have a possibility to realize such a pseudo-symmetry as one of its multicritical points. This will be left for future investigation.

It would also be worth investigating the Higgs inflation in this model, and the effect of right-handed neutrinos, which makes the perturbativity bound milder, along the line of Ref. [20].

Acknowledgements We would like to thank Dr. Toshinori Matsui for fruitful discussions. The work of YH is supported by JSPS Overseas Research Fellowships. The work of KO is partly supported by the JSPS Kakenhi Grant No. 19H01899. The work of KY is supported in part by the Grant-in-Aid for Early-Career Scientists, No. 19K14714. The work of KK is supported by Grant Korea NRF-2019R1C1CC1010050, 2019R1A6A1A10073437. H.K. thanks Professor Shin-Nan Yang and his family for their kind support through the Chin Yu chair professorship. The work of H.K. is also partially supported by the Japan Society of Promotion of Science, Grants (No. 20K03970 and 18H03708), by the Ministry of Science and Technology, R.O.C. (MOST 110-2811-M-002-500), and by National Taiwan University.

Data Availability Statement This manuscript has no associated data or the data will not be deposited. [Authors' comment: We do not have any data because this is theoretical work.]

Funded by SCOAP[3].

References

1. LIGO Scientific, Virgo Collaboration, B.P. Abbott et al., Observation of gravitational waves from a binary black hole merger. Phys. Rev. Lett. **116**(6), 061102 (2016). https://doi.org/10.1103/PhysRevLett.116.061102. arXiv:1602.03837 [gr-qc]
2. LIGO Scientific, Virgo Collaboration, B.P. Abbott et al., GW170817: observation of gravitational waves from a binary neutron star inspiral. Phys. Rev. Lett. **119**(16), 161101 (2017). https://doi.org/10.1103/PhysRevLett.119.161101. arXiv:1710.05832 [gr-qc]
3. LIGO Scientific, Virgo Collaboration, B.P. Abbott et al., GWTC-1: a gravitational-wave transient catalog of compact binary mergers observed by LIGO and Virgo during the first and second observing runs. Phys. Rev. X **9**(3), 031040 (2019). https://doi.org/10.1103/PhysRevX.9.031040. arXiv:1811.12907 [astro-ph.HE]
4. LIGO Scientific, VIRGO, KAGRA Collaboration, R. Abbott et al., Tests of general relativity with Gwtc-3. arXiv:2112.06861 [gr-qc]
5. LIGO Scientific, VIRGO, KAGRA Collaboration, R. Abbott et al., All-sky search for gravitational wave emission from scalar boson clouds around spinning black holes in Ligo O3 Data. arXiv:2111.15507 [astro-ph.HE]
6. LIGO Scientific, Virgo, 1M2H, Dark Energy Camera GW-E, DES, DLT40, Las Cumbres Observatory, VINROUGE, MASTER Collaboration, B.P. Abbott et al., A gravitational-wave standard siren measurement of the Hubble constant. Nature **551**(7678), 85–88 (2017). https://doi.org/10.1038/nature24471. arXiv:1710.05835 [astro-ph.CO]
7. NANOGrav Collaboration, Z. Arzoumanian et al., The NANOGrav 12.5 yr data set: search for an isotropic stochastic gravitational-wave background. Astrophys. J. Lett. **905**(2), L34 (2020). https://doi.org/10.3847/2041-8213/abd401. arXiv:2009.04496 [astro-ph.HE]
8. S. Blasi, V. Brdar, K. Schmitz, Has NANOGrav found first evidence for cosmic strings? Phys. Rev. Lett. **126**(4), 041305 (2021). https://doi.org/10.1103/PhysRevLett.126.041305 arXiv:2009.06607 [astro-ph.CO]
9. V. Vaskonen, H. Veermäe, Did NANOGrav see a signal from primordial black hole formation? Phys. Rev. Lett. **126**(5), 051303 (2021). https://doi.org/10.1103/PhysRevLett.126.051303 arXiv:2009.07832 [astro-ph.CO]
10. V. De Luca, G. Franciolini, A. Riotto, NANOGrav data hints at primordial black holes as dark matter. Phys. Rev. Lett. **126**(4), 041303 (2021). https://doi.org/10.1103/PhysRevLett.126.041303 arXiv:2009.08268 [astro-ph.CO]
11. Y. Nakai, M. Suzuki, F. Takahashi, M. Yamada, Gravitational waves and dark radiation from dark phase transition: connecting NANOGrav pulsar timing data and hubble tension. Phys. Lett. B **816**, 136238 (2021). https://doi.org/10.1016/j.physletb.2021.136238 arXiv:2009.09754 [astro-ph.CO]
12. A. Addazi, Y.-F. Cai, Q. Gan, A. Marciano, K. Zeng, NANOGrav results and dark first order phase transitions. Sci. China Phys.

Mech. Astron. **64**(9), 290411 (2021). https://doi.org/10.1007/s11433-021-1724-6 arXiv:2009.10327 [hep-ph]
13. C. Grojean, G. Servant, Gravitational waves from phase transitions at the electroweak scale and beyond. Phys. Rev. D **75**, 043507 (2007). https://doi.org/10.1103/PhysRevD.75.043507 arXiv:hep-ph/0607107
14. L. Leitao, A. Megevand, A.D. Sanchez, Gravitational waves from the electroweak phase transition. JCAP **10**, 024 (2012). https://doi.org/10.1088/1475-7516/2012/10/024 arXiv:1205.3070 [astro-ph.CO]
15. R. Jinno, K. Nakayama, M. Takimoto, Gravitational waves from the first order phase transition of the Higgs field at high energy scales. Phys. Rev. D **93**(4), 045024 (2016). https://doi.org/10.1103/PhysRevD.93.045024 arXiv:1510.02697 [hep-ph]
16. K. Hashino, M. Kakizaki, S. Kanemura, T. Matsui, Synergy between measurements of gravitational waves and the triple-Higgs coupling in probing the first-order electroweak phase transition. Phys. Rev. D **94**(1), 015005 (2016). https://doi.org/10.1103/PhysRevD.94.015005 arXiv:1604.02069 [hep-ph]
17. K. Kajantie, M. Laine, K. Rummukainen, M.E. Shaposhnikov, Is there a hot electroweak phase transition at $m_H \gtrsim m_W$? Phys. Rev. Lett. **77**, 2887–2890 (1996). https://doi.org/10.1103/PhysRevLett.77.2887 arXiv:hep-ph/9605288
18. M. Laine, K. Rummukainen, What's new with the electroweak phase transition? Nucl. Phys. B Proc. Suppl. **73**, 180–185 (1999). https://doi.org/10.1016/S0920-5632(99)85017-8 arXiv:hep-lat/9809045
19. Y. Hamada, H. Kawai, K.-Y. Oda, K. Yagyu, Dark matter in minimal dimensional transmutation with multicritical-point principle. JHEP **01**, 087 (2021). https://doi.org/10.1007/JHEP01(2021)087 arXiv:2008.08700 [hep-ph]
20. Y. Hamada, H. Kawai, K. Kawana, K.-Y. Oda, K. Yagyu, Minimal scenario of criticality for electroweak scale, neutrino masses, dark matter, and inflation. Eur. Phys. J. C **81**(11), 962 (2021). https://doi.org/10.1140/epjc/s10052-021-09735-z arXiv:2102.04617 [hep-ph]
21. S.R. Coleman, E.J. Weinberg, Radiative corrections as the origin of spontaneous symmetry breaking. Phys. Rev. D **7**, 1888–1910 (1973). https://doi.org/10.1103/PhysRevD.7.1888
22. H. Kawai, K. Kawana, Multi-critical point principle as the origin of classical conformality and its generalizations. arXiv:2107.10720 [hep-th]
23. J. Haruna, H. Kawai, Weak scale from Planck scale: mass scale generation in a classically conformal two-scalar system. PTEP **2020**(3), 033B01 (2020). https://doi.org/10.1093/ptep/ptz165 arXiv:1905.05656 [hep-th]
24. W.A. Bardeen, On naturalness in the standard model, in *Ontake Summer Institute on Particle Physics* (1995)
25. K.A. Meissner, H. Nicolai, Conformal symmetry and the standard model. Phys. Lett. **B648**, 312–317 (2007). https://doi.org/10.1016/j.physletb.2007.03.023 arXiv:hep-th/0612165
26. K.A. Meissner, H. Nicolai, Neutrinos, axions and conformal symmetry. Eur. Phys. J. C **57**, 493–498 (2008). https://doi.org/10.1140/epjc/s10052-008-0760-x arXiv:0803.2814 [hep-th]
27. R. Foot, A. Kobakhidze, K.L. McDonald, R.R. Volkas, A solution to the hierarchy problem from an almost decoupled hidden sector within a classically scale invariant theory. Phys. Rev. D **77**, 035006 (2008). https://doi.org/10.1103/PhysRevD.77.035006 arXiv:0709.2750 [hep-ph]
28. S. Iso, N. Okada, Y. Orikasa, Classically conformal $B-L$ extended Standard Model. Phys. Lett. B **676**, 81–87 (2009). https://doi.org/10.1016/j.physletb.2009.04.046 arXiv:0902.4050 [hep-ph]
29. S. Iso, N. Okada, Y. Orikasa, The minimal $B-L$ model naturally realized at TeV scale. Phys. Rev. D **80**, 115007 (2009). https://doi.org/10.1103/PhysRevD.80.115007 arXiv:0909.0128 [hep-ph]
30. T. Hur, P. Ko, Scale invariant extension of the standard model with strongly interacting hidden sector. Phys. Rev. Lett. **106**, 141802 (2011). https://doi.org/10.1103/PhysRevLett.106.141802 arXiv:1103.2571 [hep-ph]
31. S. Iso, Y. Orikasa, TeV scale B-L model with a flat Higgs potential at the Planck scale—in view of the hierarchy problem—. PTEP **2013**, 023B08 (2013). https://doi.org/10.1093/ptep/pts099 arXiv:1210.2848 [hep-ph]
32. C. Englert, J. Jaeckel, V. Khoze, M. Spannowsky, Emergence of the electroweak scale through the Higgs portal. JHEP **04**, 060 (2013). https://doi.org/10.1007/JHEP04(2013)060 arXiv:1301.4224 [hep-ph]
33. M. Hashimoto, S. Iso, Y. Orikasa, Radiative symmetry breaking at the Fermi scale and flat potential at the Planck scale. Phys. Rev. D **89**, 016019 (2014). https://doi.org/10.1103/PhysRevD.89.016019 arXiv:1310.4304 [hep-ph]
34. M. Holthausen, J. Kubo, K.S. Lim, M. Lindner, Electroweak and conformal symmetry breaking by a strongly coupled hidden sector. JHEP **12**, 076 (2013). https://doi.org/10.1007/JHEP12(2013)076 arXiv:1310.4423 [hep-ph]
35. M. Hashimoto, S. Iso, Y. Orikasa, Radiative symmetry breaking from flat potential in various U(1)' models. Phys. Rev. D **89**(5), 056010 (2014). https://doi.org/10.1103/PhysRevD.89.056010 arXiv:1401.5944 [hep-ph]
36. J. Kubo, K.S. Lim, M. Lindner, Electroweak symmetry breaking via QCD. Phys. Rev. Lett. **113**, 091604 (2014). https://doi.org/10.1103/PhysRevLett.113.091604 arXiv:1403.4262 [hep-ph]
37. K. Endo, Y. Sumino, A scale-invariant Higgs sector and structure of the vacuum. JHEP **05**, 030 (2015). https://doi.org/10.1007/JHEP05(2015)030 arXiv:1503.02819 [hep-ph]
38. J. Kubo, M. Yamada, Genesis of electroweak and dark matter scales from a bilinear scalar condensate. Phys. Rev. D **93**(7), 075016 (2016). https://doi.org/10.1103/PhysRevD.93.075016 arXiv:1505.05971 [hep-ph]
39. D.-W. Jung, J. Lee, S.-H. Nam, Scalar dark matter in the conformally invariant extension of the standard model. Phys. Lett. B **797**, 134823 (2019). https://doi.org/10.1016/j.physletb.2019.134823 arXiv:1904.10209 [hep-ph]
40. D. Bennett, H.B. Nielsen, Predictions for nonAbelian fine structure constants from multicriticality. Int. J. Mod. Phys. A **9**, 5155–5200 (1994). https://doi.org/10.1142/S0217751X94002090 arXiv:hep-ph/9311321
41. C. Froggatt, H.B. Nielsen, Standard model criticality prediction: top mass 173 ± 5-GeV and Higgs mass 135 ± 9-GeV. Phys. Lett. B **368**, 96–102 (1996). https://doi.org/10.1016/0370-2693(95)01480-2 arXiv:hep-ph/9511371
42. H.B. Nielsen, Predicted the Higgs Mass. Bled Workshops Phys. **13**(2), 94–126 (2012). arXiv:1212.5716 [hep-ph]
43. H. Kawai, T. Okada, Solving the naturalness problem by baby universes in the Lorentzian multiverse. Prog. Theor. Phys. **127**, 689–721 (2012). https://doi.org/10.1143/PTP.127.689 arXiv:1110.2303 [hep-th]
44. H. Kawai, Low energy effective action of quantum gravity and the naturalness problem. Int. J. Mod. Phys. A **28**, 1340001 (2013). https://doi.org/10.1142/S0217751X13400010
45. Y. Hamada, H. Kawai, K. Kawana, Evidence of the big fix. Int. J. Mod. Phys. A **29**, 1450099 (2014). https://doi.org/10.1142/S0217751X14500997 arXiv:1405.1310 [hep-ph]
46. Y. Hamada, H. Kawai, K. Kawana, Weak scale from the maximum entropy principle. PTEP **2015**, 033B06 (2015). https://doi.org/10.1093/ptep/ptv011 arXiv:1409.6508 [hep-ph]
47. Y. Hamada, H. Kawai, K. Kawana, Natural solution to the naturalness problem: the universe does fine-tuning. PTEP **2015**(12), 123B03 (2015). https://doi.org/10.1093/ptep/ptv168 arXiv:1509.05955 [hep-th]

48. K. Kannike, N. Koivunen, M. Raidal, Principle of multiple point criticality in multi-scalar dark matter models. Nucl. Phys. B **968**, 115441 (2021). https://doi.org/10.1016/j.nuclphysb.2021.115441 arXiv:2010.09718 [hep-ph]
49. A. Racioppi, J. Rajasalu, K. Selke, Multiple point criticality principle and Coleman–Weinberg inflation. arXiv:2109.03238 [astro-ph.CO]
50. XENON Collaboration, E. Aprile et al., Dark matter search results from a one ton-year exposure of XENON1T. Phys. Rev. Lett. **121**(11), 111302 (2018). https://doi.org/10.1103/PhysRevLett.121.111302. arXiv:1805.12562 [astro-ph.CO]
51. G. Bélanger, F. Boudjema, A. Goudelis, A. Pukhov, B. Zaldivar, micrOMEGAs5.0: freeze-in. Comput. Phys. Commun. **231**, 173–186 (2018). https://doi.org/10.1016/j.cpc.2018.04.027 arXiv:1801.03509 [hep-ph]
52. Planck Collaboration, N. Aghanim et al., Planck 2018 results. VI. Cosmological parameters. Astron. Astrophys. **641** A6 (2020). https://doi.org/10.1051/0004-6361/201833910. arXiv:1807.06209 [astro-ph.CO]
53. ATLAS Collaboration, Combined measurements of Higgs boson production and decay using up to 139 fb^{-1} of proton–proton collision data at $\sqrt{s} = 13$ TeV collected with the ATLAS experiment
54. D. Curtin, P. Meade, H. Ramani, Thermal resummation and phase transitions. Eur. Phys. J. C **78**(9), 787 (2018). https://doi.org/10.1140/epjc/s10052-018-6268-0 arXiv:1612.00466 [hep-ph]
55. E. Senaha, Symmetry restoration and breaking at finite temperature: an introductory review. Symmetry **12**(5), 733 (2020). https://doi.org/10.3390/sym12050733
56. R.R. Parwani, Resummation in a hot scalar field theory. Phys. Rev. D **45**, 4695 (1992). https://doi.org/10.1103/PhysRevD.45.4695. arXiv:hep-ph/9204216. [Erratum: Phys. Rev. D **48**, 5965 (1993)]
57. E.W. Kolb, M.S. Turner, *The Early Universe*, vol. 69 (1990). https://doi.org/10.1201/9780429492860
58. X. Wang, F.P. Huang, X. Zhang, Phase transition dynamics and gravitational wave spectra of strong first-order phase transition in supercooled universe. JCAP **05**, 045 (2020). https://doi.org/10.1088/1475-7516/2020/05/045 arXiv:2003.08892 [hep-ph]
59. Y. Gouttenoire, R. Jinno, F. Sala, Friction pressure on relativistic bubble walls. arXiv:2112.07686 [hep-ph]
60. C. Caprini et al., Science with the space-based interferometer eLISA. II: gravitational waves from cosmological phase transitions. JCAP **04**, 001 (2016). https://doi.org/10.1088/1475-7516/2016/04/001 arXiv:1512.06239 [astro-ph.CO]
61. C. Caprini et al., Detecting gravitational waves from cosmological phase transitions with LISA: an update. JCAP **03**, 024 (2020). https://doi.org/10.1088/1475-7516/2020/03/024 arXiv:1910.13125 [astro-ph.CO]
62. V. Guada, M. Nemevšek, M. Pintar, FindBounce: package for multi-field bounce actions. Comput. Phys. Commun. **256**, 107480 (2020). https://doi.org/10.1016/j.cpc.2020.107480 arXiv:2002.00881 [hep-ph]
63. C.L. Wainwright, CosmoTransitions: computing cosmological phase transition temperatures and bubble profiles with multiple fields. Comput. Phys. Commun. **183**, 2006–2013 (2012). https://doi.org/10.1016/j.cpc.2012.04.004 arXiv:1109.4189 [hep-ph]
64. F. Giese, T. Konstandin, J. van de Vis, Model-independent energy budget of cosmological first-order phase transitions—a sound argument to go beyond the bag model. JCAP **07**(07), 057 (2020). https://doi.org/10.1088/1475-7516/2020/07/057 arXiv:2004.06995 [astro-ph.CO]
65. R. Jinno, M. Takimoto, Probing a classically conformal B-L model with gravitational waves. Phys. Rev. D **95**(1), 015020 (2017). https://doi.org/10.1103/PhysRevD.95.015020 arXiv:1604.05035 [hep-ph]
66. J.R. Espinosa, T. Konstandin, J.M. No, G. Servant, Energy budget of cosmological first-order phase transitions. JCAP **06**, 028 (2010). https://doi.org/10.1088/1475-7516/2010/06/028 arXiv:1004.4187 [hep-ph]
67. J. Ellis, M. Lewicki, J.M. No, Gravitational waves from first-order cosmological phase transitions: lifetime of the sound wave source. JCAP **07**, 050 (2020). https://doi.org/10.1088/1475-7516/2020/07/050 arXiv:2003.07360 [hep-ph]
68. R. Peccei, H.R. Quinn, CP conservation in the presence of instantons. Phys. Rev. Lett. **38**, 1440–1443 (1977). https://doi.org/10.1103/PhysRevLett.38.1440
69. F. Wilczek, Problem of strong P and T invariance in the presence of instantons. Phys. Rev. Lett. **40**, 279–282 (1978). https://doi.org/10.1103/PhysRevLett.40.279
70. S. Weinberg, A new light boson? Phys. Rev. Lett. **40**, 223–226 (1978). https://doi.org/10.1103/PhysRevLett.40.223
71. J.E. Kim, Weak interaction singlet and strong CP invariance. Phys. Rev. Lett. **43**, 103 (1979). https://doi.org/10.1103/PhysRevLett.43.103
72. M.A. Shifman, A. Vainshtein, V.I. Zakharov, Can confinement ensure natural CP invariance of strong interactions? Nucl. Phys. B **166**, 493–506 (1980). https://doi.org/10.1016/0550-3213(80)90209-6
73. A.R. Zhitnitsky, On possible suppression of the axion hadron interactions (in Russian). Sov. J. Nucl. Phys. **31**, 260 (1980)
74. M. Dine, W. Fischler, M. Srednicki, A simple solution to the strong CP problem with a harmless axion. Phys. Lett. B **104**, 199–202 (1981). https://doi.org/10.1016/0370-2693(81)90590-6
75. J.E. Kim, G. Carosi, Axions and the strong CP problem. Rev. Mod. Phys. **82**, 557–602 (2010). https://doi.org/10.1103/RevModPhys.82.557. arXiv:0807.3125 [hep-ph]. [Erratum: Rev. Mod. Phys. **91**, 049902 (2019)]
76. G. Grilli di Cortona, E. Hardy, J. Pardo Vega, G. Villadoro, The QCD axion, precisely. JHEP **01**, 034 (2016). https://doi.org/10.1007/JHEP01(2016)034 arXiv:1511.02867 [hep-ph]